



Supplement of

LGHAP: the Long-term Gap-free High-resolution Air Pollutant concentration dataset, derived via tensor-flow-based multimodal data fusion

Kaixu Bai et al.

Correspondence to: Kaixu Bai (kxbai@geo.ecnu.edu.cn) and Jianping Guo (jpguocams@gmail.com)

The copyright of individual parts of the supplement might differ from the article licence.

21 **Section S1: Satellite-based AOD products**

22 • **MAIAC AOD product**

23 The multiangle implementation of atmospheric correction (MAIAC) is the latest algorithm used
24 for processing MODIS Collection 6 data record, providing not only land surface reflectance but AOD
25 products simultaneously with daily/1-km resolution. Since the first release of MAIAC algorithm in
26 2011 (Lyapustin et al., 2011), a variety of improvements had been made in cloud/snow detection,
27 aerosol retrieval, and atmospheric correction, and the ultimate goal was to facilitate global scale
28 processing and improve the data accuracy (Lyapustin et al., 2018). Please refer to Lyapustin et al.
29 (2018) for more details related to the main changes. The MAIAC product was named after MCD19,
30 and the AOD product was MCD19A2, which can be accessible via the Land Product Distributed Active
31 Archive Center (LP DAAC). Many validation studies had confirmed that MAIAC AOD had a
32 comparable or even better accuracy than those derived from the Dark Target and Deep Blue algorithms
33 with higher spatial resolution (Goldberg et al., 2019; Lyapustin et al., 2018; Xiao et al., 2017).
34 Consequently, this AOD product was used as the baseline dataset to help generate gap-filled high
35 resolution AOD dataset in China.

36 • **MISR AOD**

37 The Multi-angle Imaging SpectroRadiometer (MISR) is one of five science instruments aboard
38 the polar-orbiting Terra satellite. MISR observes the Earth globally at nine different view zenith angles
39 in four spectral bands (446, 558, 672, and 866 nm) with a cross-track ground spatial resolution of 275
40 m–1.1 km. Its multi-angular imaging design has enabled to retrieve AOD, surface bidirectional
41 reflectance factors, and hemispherical reflectances over a wide variety of land surface types, providing
42 an extensive dataset of global Earth observations since the early 2000 (Diner et al., 2004; Garay et al.,
43 2020; Witek et al., 2018). The characteristic of multi-angle earth observation is benefit to retrieve
44 aerosol properties more intensively (Guo et al., 2012). Detailed descriptions to the MISR aerosol
45 retrieval methodology over land, e.g., aerosol model selection and radiative transfer theory, can be
46 found in Diner et al. (2004). Compared to the nadir sensor such as MODIS, MISR is more sensitive to
47 aerosol components given the multi-angular imaging design. In this study, the latest version (V23) of

48 MISR aerosol product with the resolution of 4.4-km (Garay et al., 2020), was used to support the
49 generation of gap-filled AOD imagery.

50 • **VIIRS AOD**

51 The Visible Infrared Imaging Radiometer Suite (VIIRS) is a new instrument aboard the polar-
52 orbiting Suomi National Polar-orbiting Partnership (Suomi-NPP) spacecraft which was launched in
53 2011. As a new generation of operational moderate resolution-imaging radiometer, VIIRS has 22
54 imaging and radiometric bands covering wavelengths from 0.41 to 12.5 micrometers, providing more
55 than twenty environmental data records to continue the Earth observation mission initiated by the
56 AVHRR on NOAA and MODIS on Terra and Aqua satellites. Compared to the well-known MODIS,
57 VIIRS has finer spatial resolution with a larger swath. It can provide AOD retrievals at a resolution of
58 0.75-km (IP product) and 6-km (Environmental Data Record) (Jackson et al., 2013; Levy et al., 2013).
59 A specific aerosol retrieval algorithm was designed to infer AOD from VIIRS observations, with
60 changes not only in theoretical basis and retrieval limitations but also data quality flagging (Jackson
61 et al., 2013). Ground-based validation results indicated a generally good accuracy of VIIRS AOD
62 ($R^2=0.73$) when compared to AERONET AOD observations (Xiao et al., 2016).

63 • **AATSR AOD**

64 The Advanced Along-Track Scanning Radiometer (AATSR) is one of the Announcement of
65 Opportunity (AO) instruments onboard the European Space Agency (ESA) satellite Envisat, which
66 was primarily designed for measuring sea surface temperature (Wen et al., 2019). The AATSR was
67 designed to have seven spectral channels at wavelengths of 0.55, 0.67, 0.87, 1.63, 10.7, and 12 μm ,
68 which observes at dual view as one is the nadir direction and the other is forward direction with a
69 viewing angle of 55° from nadir view. The nadir spatial resolution is $1\text{ km} \times 1\text{ km}$ with a swath width
70 of 512 pixels (Che et al., 2016). By taking advantage of the features of dual view, AOD can be retrieved
71 from the AATSR observations both over land and ocean. Previous studies had indicated that AOD
72 from AATSR had a generally good accuracy, with R of 0.88 and RMS of 0.24 when compared with
73 AOD observations from AERONET (de Leeuw et al., 2018). In this study, we used ensemble AOD
74 product provided by Climate Change Initiative (CCI) that aggregating three new versions of AATSR

75 aerosol datasets with spatial resolution of 0.1° (ADV v3.11, ORAC v4.10, and SU v4.32) (de Leeuw
76 et al., 2018; Wen et al., 2019; Xie et al., 2018).

77 • POLDER AOD

78 The Polarization and Directionality of the Earth's Reflectance (POLDER) is a first satellite-based
79 multi-angle polarization imaging radiometer, which was developed by the French space agency CNES.
80 The third POLDER radiometer (POLDER-3) was deployed on PARASOL satellite, which was
81 operated from March 2005 to October 2013 with an Equator crossing time at 13:30 (local time).
82 POLDER-3 used a $274 \text{ pixels} \times 242 \text{ pixels}$ CCD detector array with a pixel size of $5.3 \text{ km} \times 6.2 \text{ km}$ at
83 nadir. It measures in 9 spectral channels from blue ($0.443 \mu\text{m}$) to near-infrared ($1.020 \mu\text{m}$), providing
84 the polarization measurements at $0.490 \mu\text{m}$, $0.670 \mu\text{m}$ and $0.865 \mu\text{m}$ at up to 16 different angles with
85 a size of $2100 \text{ km} \times 1600 \text{ km}$ (Formenti et al., 2018; Tan et al., 2019). With the Generalized Retrieval
86 of Atmosphere and Surface Properties (GRASP) algorithm (Dubovik et al., 2011), POLDER can
87 provide spectral AOD, fine aerosol optical depth (AODF), coarse aerosol optical depth (AODC),
88 absorbed aerosol optical depth (AAOD), the Ångström exponent (AE), complex refractive index (CRI)
89 and single scattering albedo (SSA) observations (Formenti et al., 2018; Tan et al., 2019). The inter-
90 comparison results indicated that the POLDER AOD had a similar and even higher quality when
91 compared to the MODIS AOD products derived from DT and DB algorithms (Chen et al., 2020; Tan
92 et al., 2019).

94 Section S2: Data coverage ratio weighted nonlinear correlation coefficient

95 To assess the relative contribution of each gridded AOD product to the final gap-free AOD dataset,
96 here we developed a new statistical indicator on the basis of the nonlinear correlation coefficient (NCC)
97 that was proposed in Wang et al. (2005). The NCC was derived from the concept of entropy to assess
98 the mutual information between two discrete variables. As shown in Sun et al. (2021), the NCC can
99 be calculated as follows: given two variables $x = [x_1, x_2, \dots, x_N]$ and $y = [y_1, y_2, \dots, y_N]$ with N number of
100 data pairs, we first sorted the data in each variable in an ascending order, which were then divided into
101 n equal bins. The NCC between x and y is defined as:

$$102 \quad NCC(x, y) = H(x) + H(y) - H(x, y) \quad (1)$$

103 where $H(x)$ is a revised entropy of x and can be calculated via the following equation:

$$105 \quad H(x) = - \sum_{i=1}^b \frac{n_i}{N} \log_b \frac{n_i}{N} \quad (2)$$

104

106 In Eq. (2), n_i is the number of elements in the i th bin. Similarly, the joint entropy of (x, y) can be
107 calculated as:

$$112 \quad H(x, y) = - \sum_{i=1}^b \sum_{j=1}^b \frac{n_{ij}}{N} \log_b \frac{n_{ij}}{N} \quad (3)$$

108 Considering NCC only evaluates the mutual information between two variables, which cannot
109 indicate the impact of data coverage ratio of each product, here we proposed to weight NCC by the
110 data coverage ratio of each product to account for the contribution of different data coverage, and the
111 new indicator is thus termed as weighted NCC (WNCC) which can be formulated as:

$$113 \quad WNCC = w * NCC \quad (5)$$

114 where w is the valid data coverage ratio of each product. Therefore, both data coverage ratio and
115 mutual information are accounted for to better indicate the contribution of each product to the final
116 fused dataset.

References

- 118 Che, Y., Xue, Y., Mei, L., Guang, J., She, L., Guo, J., Hu, Y., Xu, H., He, X., Di, A., Fan, C.,
119 2016. Technical note: Intercomparison of three AATSR Level 2 (L2) AOD products over China.
120 Atmos. Chem. Phys. 16, 9655–9674. <https://doi.org/10.5194/acp-16-9655-2016>
- 121 Chen, C., Dubovik, O., Fuertes, D., Litvinov, P., Lapyonok, T., Lopatin, A., Ducos, F.,
122 Derimian, Y., Herman, M., Tanré, D., Remer, L. A., Lyapustin, A., Sayer, A. M., Levy, R. C., Hsu, N.
123 C., Descloîtres, J., Li, L., Torres, B., Karol, Y., Herrera, M., Herreras, M., Aspetsberger, M.,
124 Wanzenboeck, M., Bindreiter, L., Marth, D., Hangler, A. and Federspiel, C.: Validation of GRASP
125 algorithm product from POLDER/PARASOL data and assessment of multi-angular polarimetry
126 potential for aerosol monitoring, Earth Syst. Sci. Data, 12(4), 3573–3620, doi:10.5194/essd-12-3573-
127 2020, 2020.
- 128 de Leeuw, G., Sogacheva, L., Rodriguez, E., Kourtidis, K., Georgoulas, A. K., Alexandri, G.,
129 Amiridis, V., Proestakis, E., Marinou, E., Xue, Y. and Van Der A, R.: Two decades of satellite
130 observations of AOD over mainland China using ATSR-2, AATSR and MODIS/Terra: Data set
131 evaluation and large-scale patterns, Atmos. Chem. Phys., 18(3), 1573–1592, doi:10.5194/acp-18-
132 1573-2018, 2018.
- 133 Diner, D.J., Martonchik, J. V., Kahn, R.A., Pinty, B., Gobron, N., Nelson, D.L., Holben, B.N.,
134 2005. Using angular and spectral shape similarity constraints to improve MISR aerosol and surface
135 retrievals over land. Remote Sens. Environ. 94, 155–171. <https://doi.org/10.1016/j.rse.2004.09.009>
- 136 Dubovik, O., Herman, M., Holdak, A., Lapyonok, T., Tanré, D., Deuzé, J. L., Ducos, F., Sinyuk,
137 A. and Lopatin, A.: Statistically optimized inversion algorithm for enhanced retrieval of aerosol
138 properties from spectral multi-angle polarimetric satellite observations, Atmos. Meas. Tech., 4(5),
139 975–1018, doi:10.5194/amt-4-975-2011, 2011.
- 140 Formenti, P., Mbemba Kabuiku, L., Chiapello, I., Ducos, F., Dulac, F. and Tanré, D.: Aerosol
141 optical properties derived from POLDER-3/PARASOL (2005–2013) over the western Mediterranean
142 Sea – Part 1: Quality assessment with AERONET and in situ airborne observations, Atmos. Meas.
143 Tech., 11(12), 6761–6784, doi:10.5194/amt-11-6761-2018, 2018.
- 144 Garay, M. J., Witek, M. L., Kahn, R. A., Seidel, F. C., Limbacher, J. A., Bull, M. A., Diner, D.
145 J., Hansen, E. G., Kalashnikova, O. V., Lee, H., Natan, A. M. and Yu, Y.: Introducing the 4.4 km

146 spatial resolution Multi-Angle Imaging SpectroRadiometer (MISR) aerosol product, *Atmos. Meas.*
147 *Tech.*, 13(2), 593–628, doi:10.5194/amt-13-593-2020, 2020.

148 Goldberg, D. L., Gupta, P., Wang, K., Jena, C., Zhang, Y., Lu, Z. and Streets, D. G.: Using
149 gap-filled MAIAC AOD and WRF-Chem to estimate daily PM_{2.5} concentrations at 1 km resolution
150 in the Eastern United States, *Atmos. Environ.*, 199(November 2018), 443–452,
151 doi:10.1016/j.atmosenv.2018.11.049, 2019.

152 Guo, J., Gu, X., Cheng, T., Xie, D. and Chen, H.: Regional trend analysis of the aerosol optical
153 depth comparing to MODIS and MISR aerosol products, in 2012 IEEE International Geoscience and
154 Remote Sensing Symposium, pp. 3654–3657, IEEE., 2012.

155 Jackson, J. M., Liu, H., Laszlo, I., Kondragunta, S., Remer, L. A., Huang, J. and Huang, H.-C.:
156 Suomi-NPP VIIRS aerosol algorithms and data products, *J. Geophys. Res. Atmos.*, 118(22), 12,673-
157 12,689, doi:10.1002/2013JD020449, 2013.

158 Levy, R. C., Mattoo, S., Munchak, L. A., Remer, L. A., Sayer, A. M., Patadia, F. and Hsu, N.
159 C.: The Collection 6 MODIS aerosol products over land and ocean, *Atmos. Meas. Tech.*, 6(11), 2989–
160 3034, doi:10.5194/amt-6-2989-2013, 2013.

161 Lyapustin, A., Martonchik, J., Wang, Y., Laszlo, I. and Korkin, S.: Multiangle implementation
162 of atmospheric correction (MAIAC): 1. Radiative transfer basis and look-up tables, *J. Geophys. Res.*,
163 116(D3), D03210, doi:10.1029/2010JD014985, 2011.

164 Lyapustin, A., Wang, Y., Korkin, S. and Huang, D.: MODIS Collection 6 MAIAC algorithm,
165 *Atmos. Meas. Tech.*, 11(10), 5741–5765, doi:10.5194/amt-11-5741-2018, 2018.

166 Sun, Z., Chang, N. Bin, Chen, C. F., Mostafiz, C. and Gao, W.: Ensemble learning via higher
167 order singular value decomposition for integrating data and classifier fusion in water quality
168 monitoring, *IEEE J. Sel. Top. Appl. Earth Obs. Remote Sens.*, 14, 3345–3360,
169 doi:10.1109/JSTARS.2021.3055798, 2021.

170 Tan, Y., Li, E., Zhang, Z., Lin, X., Chi, Y., Zhou, L., Wu, C. and Wang, Q.: Validation of
171 POLDER-3/GRASP aerosol products using AERONET measurements over China, *Atmos. Environ.*,
172 215(April), 116893, doi:10.1016/j.atmosenv.2019.116893, 2019.

173 Wang, Q., Shen, Y., and Zhang, J. Q.: A nonlinear correlation measure for multivariable data
174 set, *Phys. D*, 3–4, 287–295, doi:10.1016/j.physd.2004.11.001, 2005.

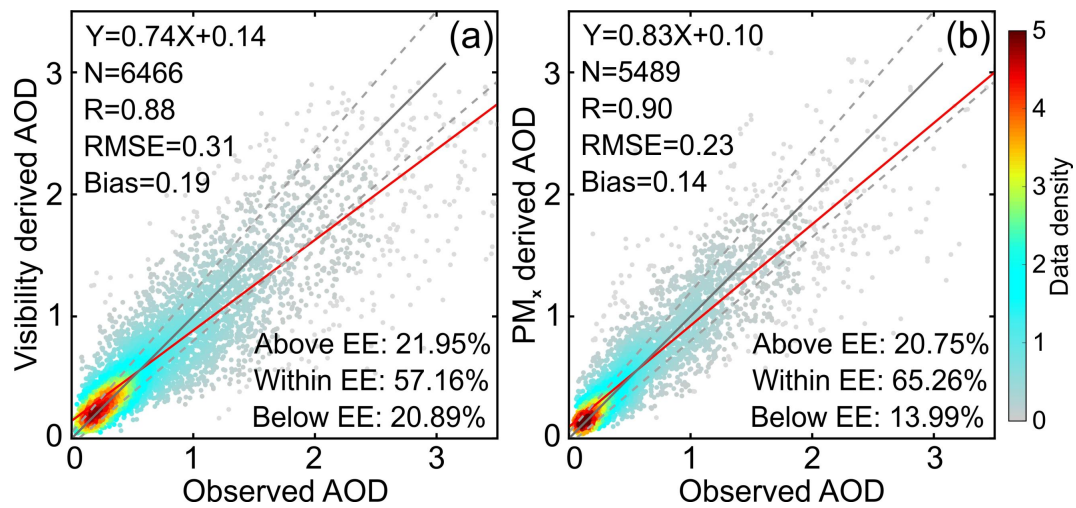
Wen, Y. N., Che, Y. H., Guang, J., Xie, Y. Q., Shi, Z., Zhang, Y. and Li, Z. Q.: VALIDATION of AEROSOL PRODUCTS from ESA/AATSR over CHINA and AOD FUSION BASED on UNCERTAINTIES, *Int. Arch. Photogramm. Remote Sens. Spat. Inf. Sci. - ISPRS Arch.*, 42(3/W9), 181–185, doi:10.5194/isprs-archives-XLII-3-W9-181-2019, 2019.

Witek, M. L., Garay, M. J., Diner, D. J., Bull, M. A. and Seidel, F. C.: New approach to the retrieval of AOD and its uncertainty from MISR observations over dark water, *Atmos. Meas. Tech.*, 11(1), 429–439, doi:10.5194/amt-11-429-2018, 2018.

Xiao, Q., Zhang, H., Choi, M., Li, S., Kondragunta, S., Kim, J., Holben, B., Levy, R.C., Liu, Y., 2016. Evaluation of VIIRS, GOCI, and MODIS Collection 6 AOD retrievals against ground sunphotometer observations over East Asia. *Atmos. Chem. Phys.* 16, 1255–1269. <https://doi.org/10.5194/acp-16-1255-2016>

Xiao, Q., Wang, Y., Chang, H. H., Meng, X., Geng, G., Lyapustin, A. and Liu, Y.: Full-coverage high-resolution daily PM_{2.5} estimation using MAIAC AOD in the Yangtze River Delta of China, *Remote Sens. Environ.*, 199(March), 437–446, doi:10.1016/j.rse.2017.07.023, 2017.

Xie, Y., Xue, Y., Che, Y., Guang, J., Mei, L., Voorhis, D., Fan, C., She, L. and Xu, H.: Ensemble of ESA/AATSR Aerosol Optical Depth Products Based on the Likelihood Estimate Method with Uncertainties, *IEEE Trans. Geosci. Remote Sens.*, 56(2), 997–1007, doi:10.1109/TGRS.2017.2757910, 2018.



194

195 **Figure S1.** Scatter plots between ground AOD observations and AOD inferred from (a) atmospheric
 196 visibility and (b) air pollutants concentration.

197

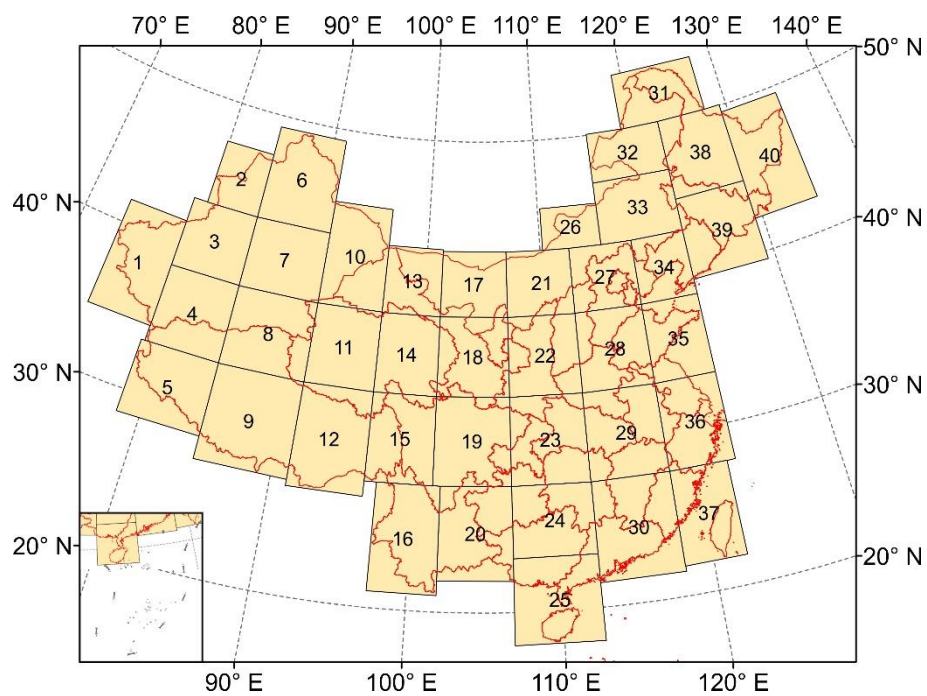


Figure S2. Spatial distribution of 40 subregions that was divided to facilitate AOD gap filling in the mainland China.

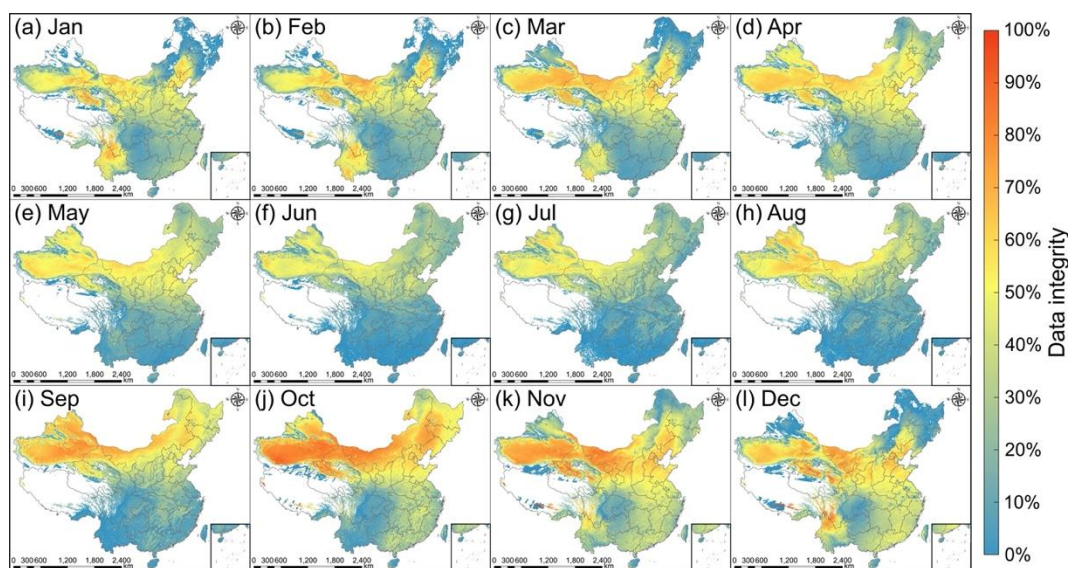


Figure S3. Monthly mean data integrity of AOD from Terra/MODIS in China during the period of 2000 to 2020.

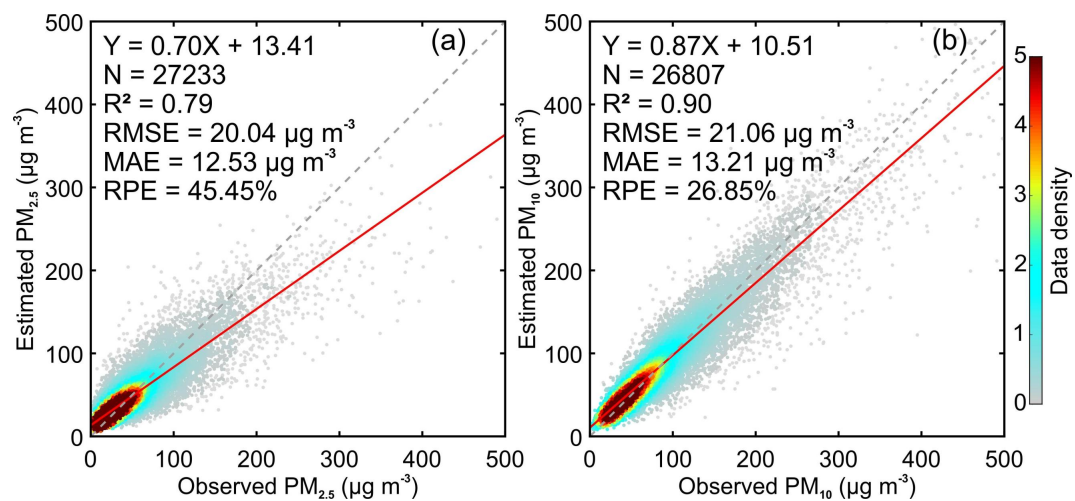


Figure S4. Sample-based cross validation accuracy of random forest models for (a) PM_{2.5} and (b) PM₁₀ mapping.

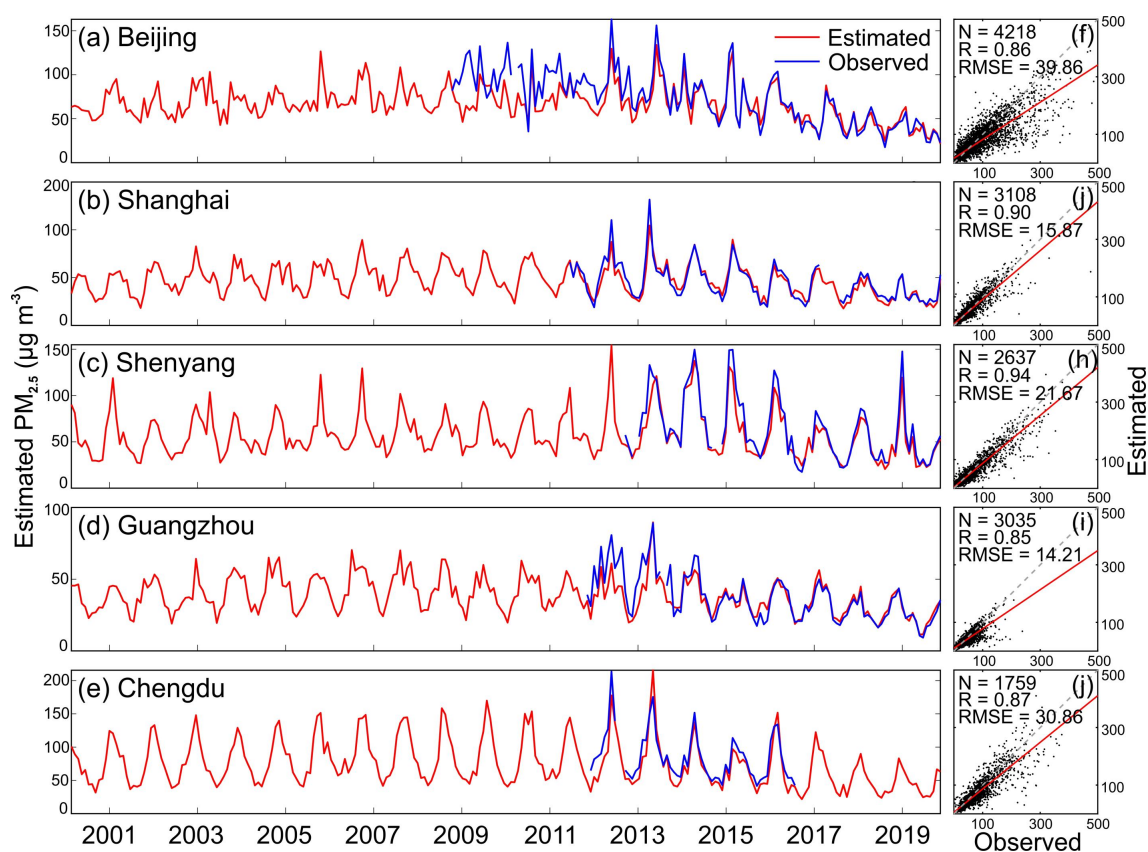


Figure S5. Comparison of SCHAP PM_{2.5} time series with measurements from United States Embassy in China. (a–e) Temporal variations of monthly PM_{2.5} concentration and (f–j) the associated daily scatter plots.

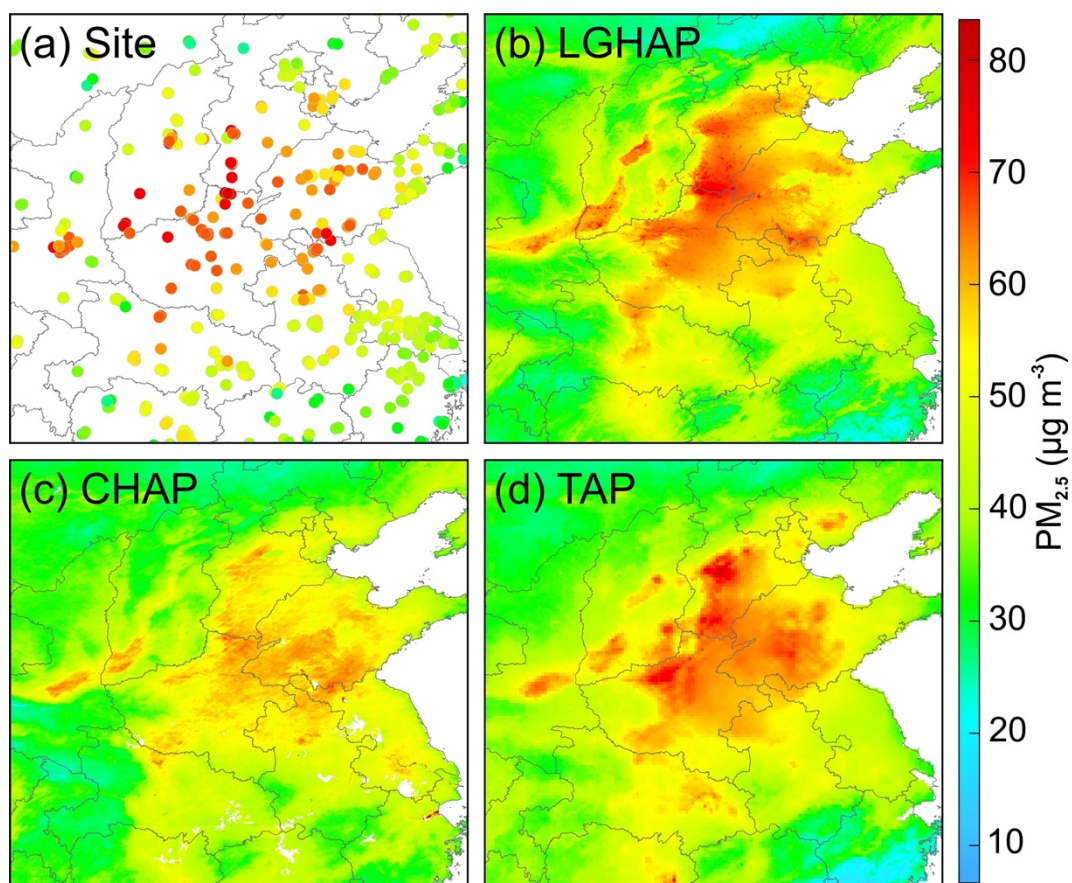


Figure S6. Comparison of spatial distribution of annual mean $PM_{2.5}$ concentration in 2019 in eastern China.

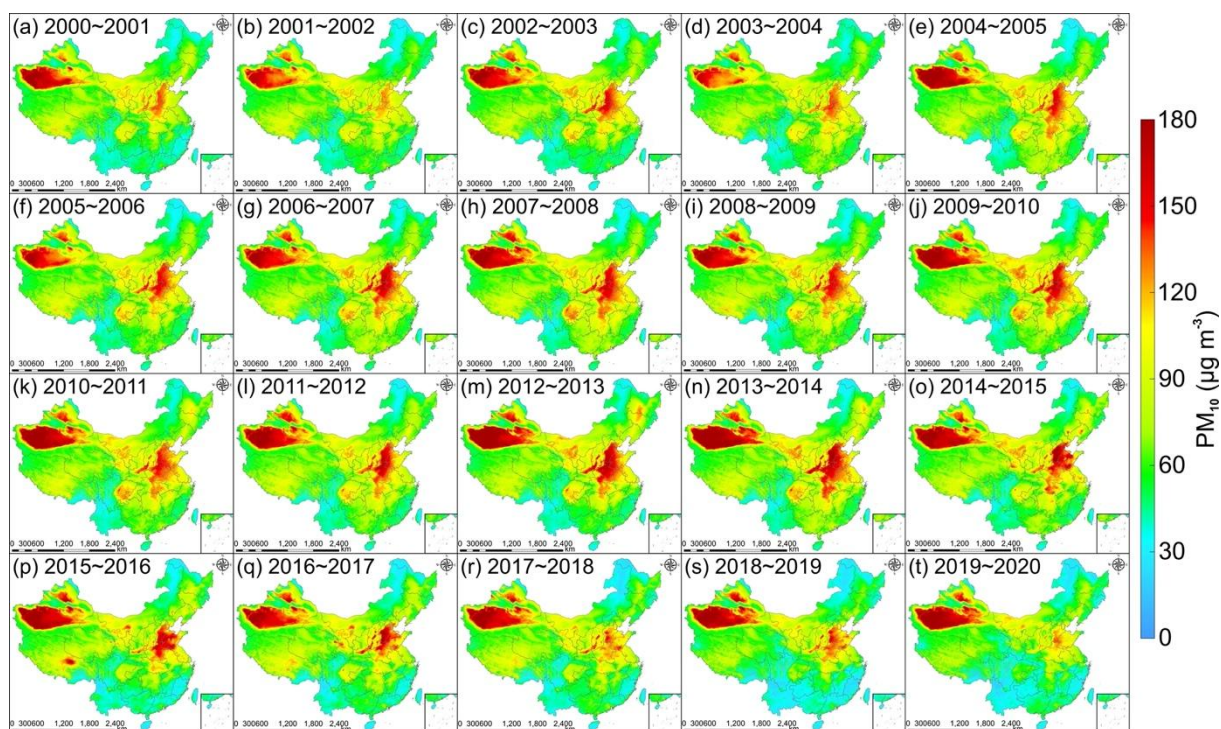


Figure S7. Spatial distribution of wintertime (September to February) averaged PM_{10} concentration from SCHAP during 2000 to 2020 in China.

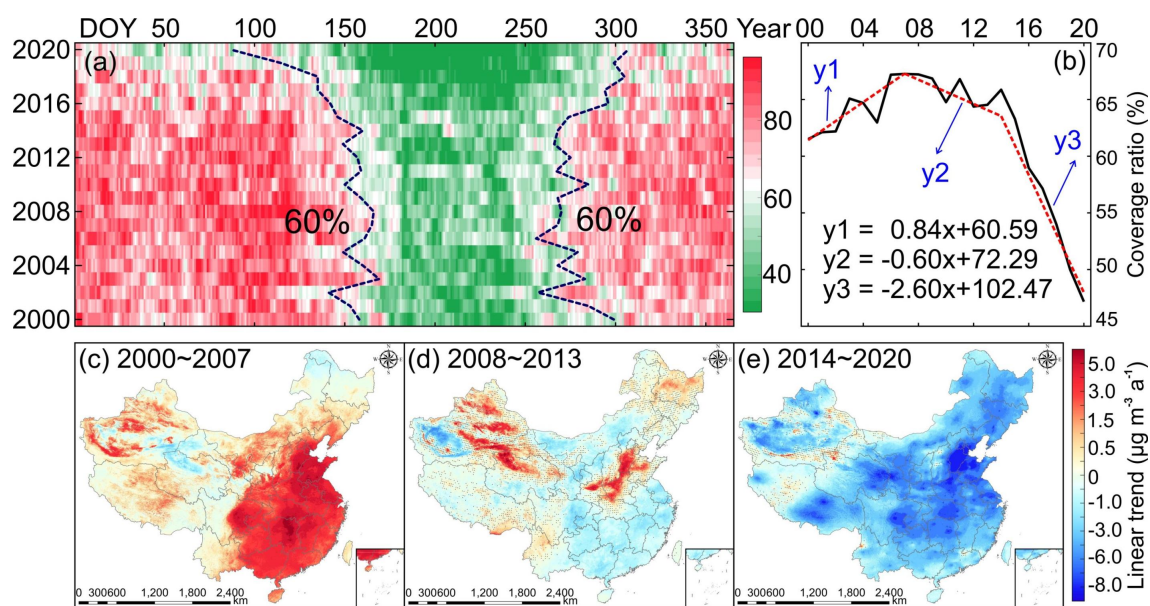


Figure S8. Temporal variations of the proportion of land areas covered with PM₁₀ concentration exceeding 50 $\mu\text{g m}^{-3}$ and PM₁₀ trends during three different periods. (a) Temporal variations of the land coverage ratio with daily PM₁₀ concentration exceeding 50 $\mu\text{g m}^{-3}$ from 2000 to 2000. (b) same as (a) but for annual mean PM₁₀ concentration. (c–e) PM₁₀ trends during periods of 2000–2007, 2008–2013, and 2014–2020. The dotted regions imply trend estimations are statistically insignificant at the 95% confidence interval.

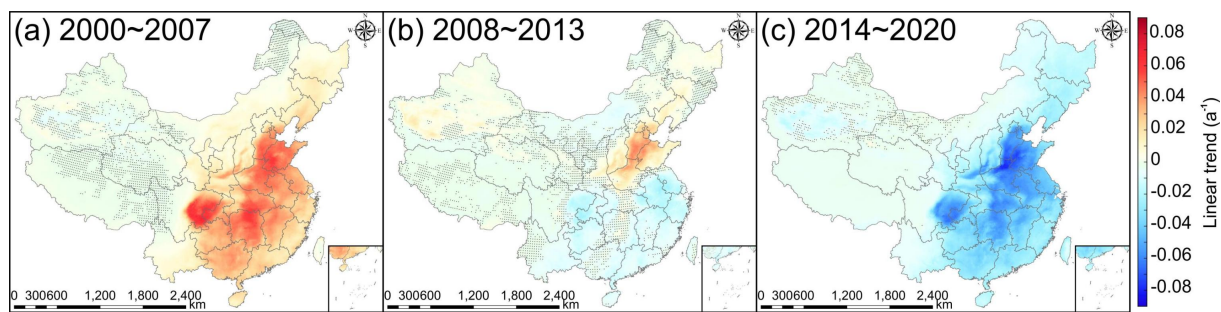


Figure S9. AOD trends during periods of (a) 2000–2007, (b) 2008–2013, and (c) 2014–2020. The dotted regions imply trend estimations are statistically insignificant at the 95% confidence interval.